Final Report for SCEC project, "Probabilities for Jumping Fault Segment Stepovers" 2007, $30,000, PI: B.E. Shaw

In the last year, one paper has been published, one more paper is in press, and two more papers have been submitted for publication. Below, some results of the papers are mentioned.

"Probabilities for jumping fault segment stepovers", [Shaw, B.E. and J.H. Dieterich, 2007], *Geophysical Research Letters, 34* **L01307, doi:10.1029/2006GL027980** . Seismic hazard analysis relies heavily on the segmentation of faults. The ability of ruptures to break multiple segments has a big impact on estimated hazard. Current practice for estimating multiple segment breakage relies on panels of experts voting on their opinions for each case. Here, we explore the probability of elastodynamic ruptures jumping segment stepovers in numerical simulations of segmented fault systems. We find a simple functional form for the probability of jumping a segment stepover as a function of stepover distance: an exponential falloff with distance. We suggest this simple parameterization of jumping probabilities, combined with sparse observational data to fix the lengthscale parameter, as a new approach to estimating multisegment earthquake hazard.

Figure 1a shows the probability of jumping a segments stepover for all the pairs of segments as a function of stepover separation distance. It shows as well a mean fit to the probability.

Plotting the log of the jump probability versus the linear distance of separation, Figure 1b shows a key result: the jump probability is seen to fall off exponentially at short distances, followed by a slower exponential falloff at larger distances. Specifically, we find

$$p(r) = e^{-r/r_0} + \epsilon(e^{-r/r_1} - e^{-r/r_0}) \tag{1}$$

is a good fit to the probability p distribution dependence on distance r, with $\epsilon \ll 1$ and $r_0 < r_1$. This provides a one parameter fit r_0 at short distances, a fitting which is likely to be sufficient for hazard purposes. A further fit of a constant level ϵ at intermediate distances $r_0 < r < r_1$, and r_1 at large distances $r_1 < r$ can be made as well. Note that the probability distribution has the important continuity property tha t at zero distance the jump probability is unity.

"Afterslip and aftershocks in the rate-and-state friction law", [Helmstetter and Shaw, 2007], submitted. We study how a stress perturbation generated by a mainshock affects a fault obeying the rate-state friction law, using a simple slider)block system. Depending on the model parameters and on the initial stress, the fault exhibits aftershocks, slow earthquakes, or decaying afterslip. We found several regimes with slip rate decaying as a power-law of time, with different characteristic times and exponents. The behavior of the rate-state friction law is thus far more complex than described by the "steady-state" approximation frequently used to fit afterslip data. The fault reaches steady-state only at very large times, when slip rate has decreased to the tectonic loading rate. The complexity of the model makes it unrealistic to invert for the friction law parameters from afterslip data. We modeled afterslip measurements for 3 earthquakes using the complete rate-and-state law, and found a huge variety of model parameters that can fit the data. In particular, it is impossible to distinguish the stable velocity strengthening regime ($A > B$) from the (potentially) unstable velocity weakening regime ($A < B$). Therefore, it is not necessary to involve small scale spatial or temporal fluctuations of friction parameters A or B in order to explain the transition between stable sliding and seismic slip. In addition to B/A and stiffness k/k_c, the fault behavior is strongly controlled by stress levels following an event. Stress heterogeneity can thus explain part of the variety of postseismic behaviors observed in nature. Afterslip induces a progressive reloading of faults that are not slipping, which

can trigger aftershocks. Using the relation between stress and seismicity derived from the rate-and-state friction law, we estimate the aftershock rate triggered by co- and postseismic slip. Aftershock rate does not simply scale with stress rate, but exhibits different characteristic times and sometimes a different power-law exponent. Afterslip is thus a possible candidate to explain observations of aftershock rate decaying as a power-law of time with an Omori exponent that can be either smaller or larger than 1. Progressive unloading due to afterslip can also produce delayed seismic quiescence.

Figure 2a,b shows a phase diagram of the behaviors. Figure 2c shows how different aftershock exponents can be obtained.

"Slip-Length Scaling in Large Earthquakes: The Role of Deep Penetrating Slip Below the Seismogenic Layer", [Shaw and Wesnousky, 2008], *Bulletin of the Seismological Society of America,* **in press.** Coseismic slip is observed to increase with earthquake rupture length for lengths far beyond the lengthscale set by the seismogenic layer. The observation, when interpreted within the realm of static dislocation theory and the imposed limit that slip be confined to the seismogenic layer, implies that earthquake stress drop increases as a function of rupture length for large earthquakes and, hence, that large earthquakes differ from small. Here a three dimensional elastodynamic model is applied to show that the observed increase in coseismic slip with rupture length may be satisfied while maintaining constant stress drop across the entire spectrum of earthquake sizes when slip is allowed to penetrate below the seismogenic layer into an underlying zone characterized by velocity-strengthening behavior. Is this deep coseismic slip happening during large earthquakes? We point to a number of additional associated features of the model behavior which are potentially observable in the Earth. These include the predictions that a substantial fraction, of order a third of total coseismic moment, is due to slip below the seismogenic layer, and that slip below the seismogenic layer should be characterized by long risetimes and a dearth of high frequency motion. The slip-length scaling is illustrated in Figure 3. The coseismic penetration of slip deep below the seismogenic layer, the cause of the deep effective W, is shown in Figure 4.

"Quantifying Natural Fault Geometry: Statistics of Splay Fault Angles", [Ando, Shaw and Scholz, 2008], submitted. Faults do not act as isolated objects, but rather as parts of complex fault systems. Quantifying the geometry of fault systems remains an important and in many ways an unsolved problem. Here, we propose a new approach to the problem, using objective criteria to match geometrical objects to mapped faults. Specifically, we focus on a geometrical object of a branching fault, and numerically fit with a cost function the mapped fault system to this geometrical object. This approach allows for a systematic, unbiased, quantitative measure of an aspect of fault system geometry. Fitting a "Y" shaped object using a cost function to dextral faults in California, we find a number of significant results. (1) The largest angle of the branch structure is generally very close to $180\,\mathrm{deg}$, implying the branch is a splay fault off the primary through going fault. (2) The distribution of the smallest angle, the splay angle, has a peak near $\pm 17\,\mathrm{deg}$, symmetric about the primary fault. (3) These features appear independent of scale. These results are not yet explained by any theory, and pose new questions and constraints for the physics of fault system formation and behavior. Figure 5 shows branches fit in California as a scale of $20km$. Figure 6 shows the distribution of branch angles across different scale lengths.

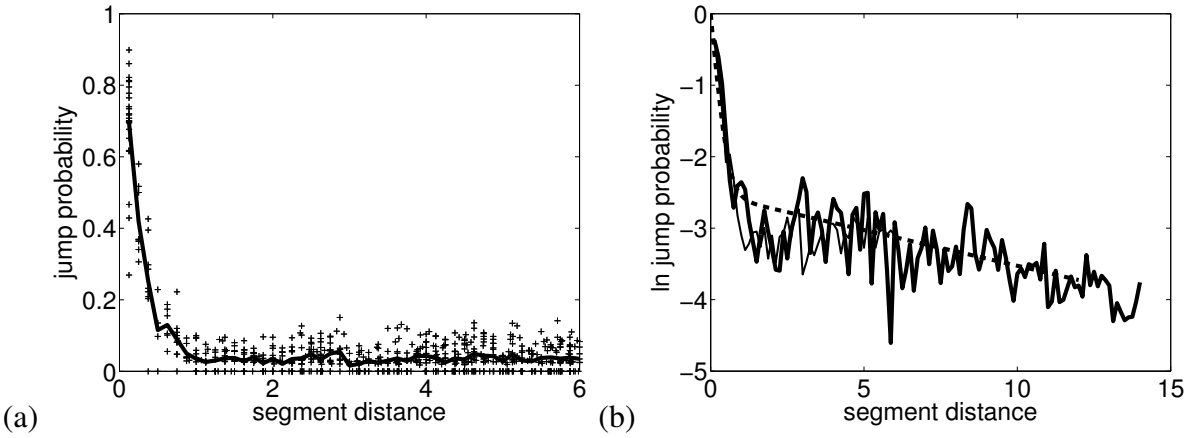

Figure 1: (a) Scatter plot of jump probabilities as a function of segment separation distance. Only segments with fault perpendicular separation distance at least as large as fault parallel separation distance are shown. Zero probability pairs are included as well, allowing for mean jump probability to be calculated, shown with solid line. (b) Functional form of mean jumping probability. Log jump probability versus linear distance. Straight line indicates exponential falloff. Functional form fit with two exponentials, one fast falloff at short distance, and one slower falloff at large distance. Dashed line shows exponential falloff Equation (1) fit with parameters $r_0 = .2$, $\epsilon = .08$, $r_1 = 10$. The two different thickness lines show two different domain sizes; they are hard to distinguish, and show the lack of dependence on domain size. From [Shaw and Dieterich, 2007].

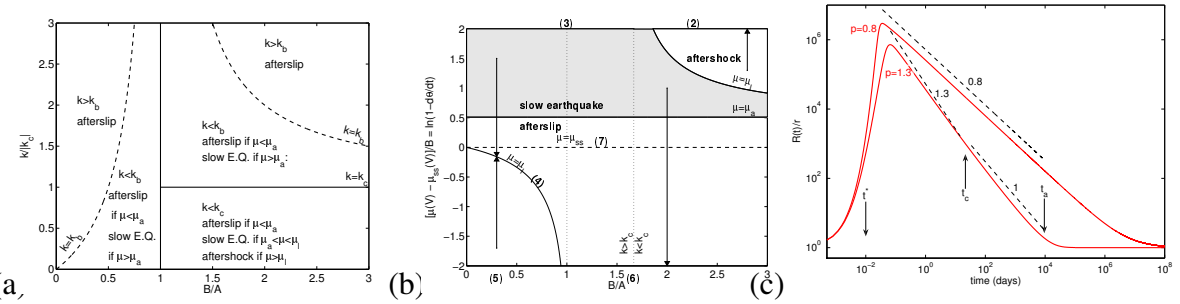

Figure 2: (a) Phase diagram of different postseismic behaviors as a function of B/A and $k/|k_c|$. (b) Friction or state variable relative to steady state as a function of B/A for $k = 0.4k_B$ and $\dot{\tau}_l = 0$, and the resulting behaviors in this phase space. Also shown are limits for acceleration and instability, and trajectories in this space (arrows). Numbers in brackets refer to asymptotic solutions discussed in the paper. (c) Seismicity rate triggered by a continuous stress change given by $\dot{\tau} = \dot{\tau}_0/(1 + t/t^*)^\beta$ with $\beta = 0.8$ (top) or $\beta = 1.3$ (bottom), $R_0 = r$, and $m = 10$. For $\beta = 1.3$, the crossover time t_c is 21.5 days, and marks the transition between a $\sim 1/t^\beta$ decay of seismicity rate for $t_m < t < t_c$ to the long time $\sim 1/t$ decay. For $\beta = 0.8$, seismicity rate is proportional to stressing rate after the end of the accelerating phase for $t > t_m$. From [Helmstetter and Shaw, 2007].

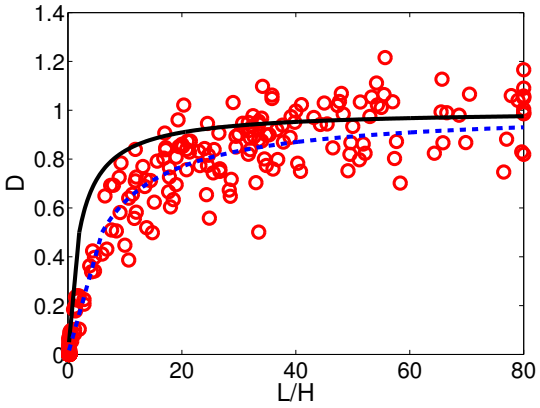

Figure 3: Average surface slip D versus rupture length L for large surface rupturing events in a three dimensional scalar elastodynamic model. Length L is scaled by the seismogenic width H showing the aspect ratio of the ruptures. Individual circles are for individual rupture events. Solid curve is with $W = H$. Dashed line shows fit for larger $W = 3H$. From [Shaw and Wesnousky, 2008].

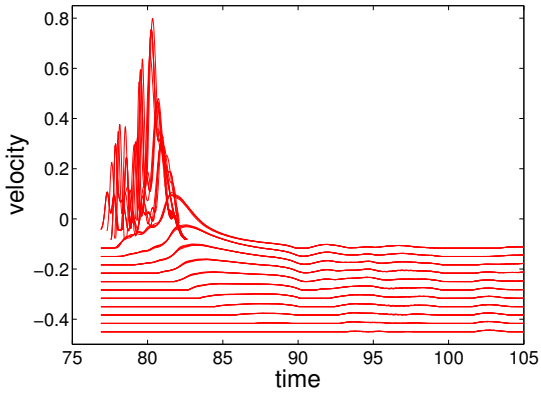

Figure 4: Velocity as a function of time for an example model large event on an array of velocity meters. Array is placed along strike around epicenter, down depth of fault. For ease in visualization, velocity is offset proportional to depth z, with offset$= .1z/H$. At each depth 5 velocity meters laterally are displaced at spacing $H/6$ around the hypocenter along strike direction; width of line gives sense of spread in velocities along-strike near epicenter. In the depth direction 14 of these lateral velocity meter lines are shown. Note high frequency motions at shallow depths, in addition to low frequency component, while motion at depth is mainly low frequency. Only nonzero velocities are plotted. Note delay of onset of motion at increased depths, as slip is driven deeper, but also note substantial coseismic slip on stably sliding lower fault. Units are dimensionless; for time, it is the time is takes a wave propagating at the shear wave velocity to propagate the seismogenic crust depth $H-$ thus a time of unity corresponds to around 5 seconds for a $3km/sec$ shear wave propagating across $15km$. For velocity, unit corresponds to the stress drop divided by the shear modulus times the shear velocity, a number around $.3m/sec$ for typical Earth values. From [Shaw and Wesnousky, 2008].

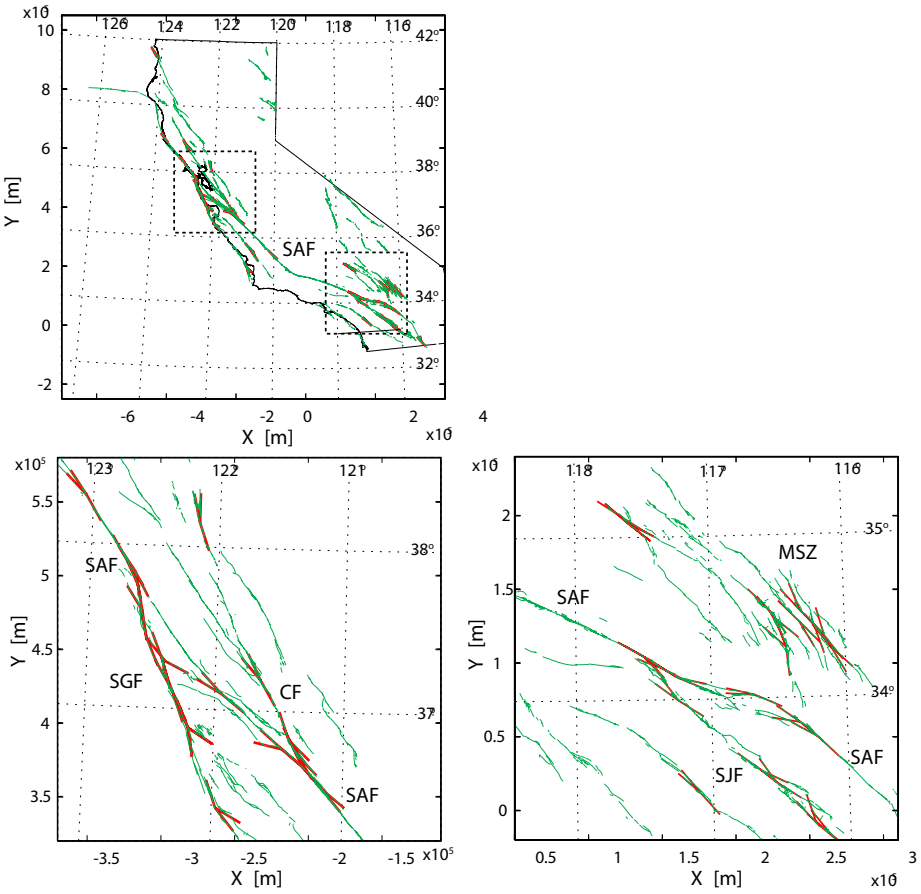

Figure 5: Surface faults and fitted fault geometry. Plots for (a) the entire California and the zooms of the boxed areas for (b) northern and (c) southern California. Green and red lines represent catalogued faults and fitted fault geometry (test function) respectively. R=20km. From [Ando, Shaw and Scholz, 2008].

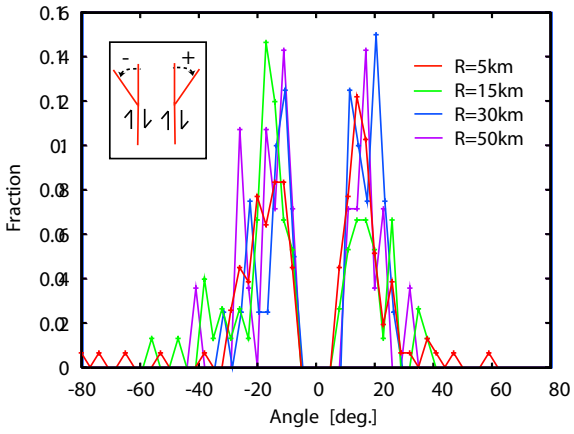

Figure 6: Statistics of splay angles. (a) Probability distribution of angles for different scales. Plot was made at intervals of 3 deg. The medians of the cases of R=5, 15, 30 and 50km ar e -17/16, -17/18, -12/16 and -17/17 for left/right-hand side branches defined in the inset. From [Ando, Shaw and Scholz, 2008].